

University of Dundee

Development of an acquisition system for high deformation barriers using low-cost IMU sensors and Image Analysis

Previtali, Marco; Ciantia, Matteo; Castellanza, Riccardo ; Crosta, Giovanni B.

Publication date:
2023

Document Version
Peer reviewed version

[Link to publication in Discovery Research Portal](#)

Citation for published version (APA):

Previtali, M., Ciantia, M., Castellanza, R., & Crosta, G. B. (2023). *Development of an acquisition system for high deformation barriers using low-cost IMU sensors and Image Analysis*. Paper presented at Geo-Resilience 2023, Cardiff , United Kingdom.

General rights

Copyright and moral rights for the publications made accessible in Discovery Research Portal are retained by the authors and/or other copyright owners and it is a condition of accessing publications that users recognise and abide by the legal requirements associated with these rights.

- Users may download and print one copy of any publication from Discovery Research Portal for the purpose of private study or research.
- You may not further distribute the material or use it for any profit-making activity or commercial gain.
- You may freely distribute the URL identifying the publication in the public portal.

Take down policy

If you believe that this document breaches copyright please contact us providing details, and we will remove access to the work immediately and investigate your claim.



Development of an acquisition system for high deformation barriers using low-cost IMU sensors and Image Analysis

Marco PREVITALI¹, Matteo CIANTIA¹, Riccardo CASTELLANZA², Giovanni CROSTA²

¹University of Dundee, Dundee, United Kingdom

²University of Milano-Bicocca, Milano, Italy

Corresponding author: Marco Previtali (m.z.previtali@dundee.ac.uk)

Abstract

Meso and full-scale impact tests have historically been used to assess the capacity of high-deformation barriers used against natural hazards and to validate numerical models. However, the data acquired from such experiments is typically limited to peak barrier elongation and occasionally force-time-displacement curves acting on specific structural elements. In rare occasions, complex and expensive procedures such as 4D photogrammetry are employed. Herein, a procedure is developed to obtain a barrier deformation data in three dimensions using low-cost MEMS sensors and consumer-grade cameras. The procedure is validated against LIDAR data for both quasi-static and dynamic conditions.

Keywords: Natural hazard, Physical model, Low-cost sensor, Model validation

1. Introduction

The mitigation of natural hazards, such as rockfall, debris flows, avalanches, etc. is often carried out through high-deformation structures, i.e. flexible protection systems. For industry purposes, international guidelines (EOTA, 2013) prescribe the recording of Maximum and Service impact Energy Levels (MEL and SEM) and of the peak mesh deformation. In recent years, academics have been recording additional data such as boulder deceleration (Gao, Al-Budairi and Steel, 2018), load on structural elements (Buzzi et al., 2013) in order to calibrate numerical models (Thoeni et al., 2013, Previtali et al., 2021). Inertial measurement units (IMUs) have also seen some use, due to the low costs associated to their development, deployment and upkeep (Pieš and Hájoský, 2018; Yan et al., 2019). Due to the lack of readily available and affordable commercial solutions, some authors proposed sensors built out of MEMS consumer grade components (Niklaus et al., 2017; Coombs et al., 2019). The combination of multiple high-speed camera viewpoints has been employed for 4D photogrammetric reconstruction (Caviezel et al., 2019), stereo camera deformation analysis (Ferrero, Segalini and Umili, 2015) and 3D visual hull fragment reconstruction (Guccione et al., 2020).

Unfortunately, the solutions provided in the literature often require expensive hardware (e.g. 4D photogrammetry requires high-speed and high-resolution cameras) or technical expertise (i.e. defining communication protocols). Depending on the time scale of the process, high-speed cameras can be substituted for commercial grade phone cameras, pi-cameras (e.g. IMX219) or other alternatives (Bruno et al., 2020). It is important to note that commercial solutions typically include video improving algorithms, that can produce uneven framerate, artificial blur, smoothing, etc.. Lossy video compression can also introduce its own set of issues. For the purpose of this paper, chroma subsampling (e.g. JPEG) and frame interpolation (e.g. MPEG4) should be avoided (van den Branden Lambrecht and Christian J, 2001). Regarding the IMU, the components proposed by Niklaus et al. (2017) has been used the base of the sensor. However, to allow people with no background in electrical engineering to reproduce the sensor, breakout boards are used instead of the MEMS themselves. All the components can be assembled with jumper cables and glued to the barrier.

In the following, a procedure to obtain the discrete displacement of an arbitrary number of targets from multiple cameras is described. Three tests were carried out: (i) slow and (ii) dynamic deformation of a cloth surface. The IMU sensors are placed in the same position of the targets in order to provide redundancy for frames in which image-based tracking is lost. LIDAR sensing is used to validate the procedure.

2. The data acquisition procedure

2.1 Image analysis

Coloured targets, i.e. markers, are placed on top of the deforming surface, avoiding environmental colours. Multiple cameras are placed facing the object from various positions. In each frame, the markers are separated from the background through HSV space segmentation: the image is first converted into Hue-Saturation-Value

(HSV) colour space. Successively, six thresholds are defined to produce a mask. Typically, low saturation values are characteristic of over and underexposed frames, that can be improved by reducing the frame opening time and camera ISO, respectively. Depending on the surface reflection and scattering, patches of colour within the desired hue threshold and can appear. Having high saturation values in the markers helps to alleviate this phenomenon. Figure 1 shows the procedure applied to 6 red markers on a cloth within the software MATLAB, using the Color Thresholder app, although it is easily replicable with open-source codes such as OpenCV (Bradski, 2000). The position of the targets is obtained from the centroid of the regions created by the hue-based mask. Finally, James Munkres' variant of the Hungarian assignment algorithm (Munkres, 1957) is used to match the positions of the targets to a list of tracks by minimizing the combined costs of Euclidean distance (i.e. how far the closest detected position is from a given track) and not assignment (i.e. how much the algorithm should try to match the position to an existing track). If a position cannot be matched to any existing track, a new one is created. As the target of a given track might momentarily disappear during the test, the Kalman filter is used to predict where its updated position should be, in order to match it with its previous track in case it reappears. Depending on the lighting conditions of the scene, using different colours for markers allows for more aggressive non-assignment weights.

A

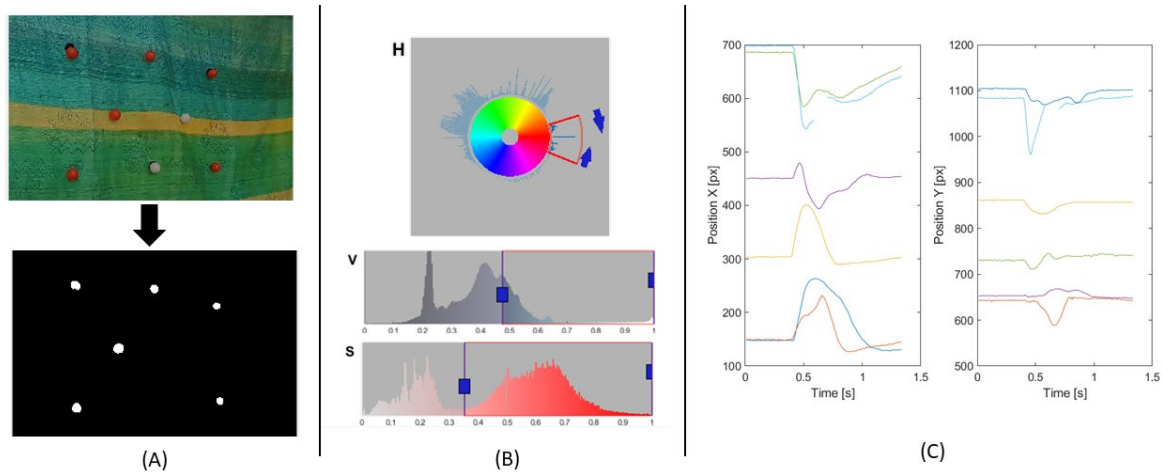


Figure 1: (A) Image binarization using the (B) HSV-space mask. (C) Evolution of the target positions in the image during the test.

Assuming the lens distortion is negligible after camera resectioning correction, and the position and orientation is either manually measured or obtained from stereo calibration, the 3D position of each marker can be estimated for each frame through triangulation. The main advantage of using Particle Tracking Velocimetry (PTV) over classic stereo camera and photogrammetry algorithms is that by limiting the number of targets and separating the point matching and triangulation procedures, it is possible to obtain reliable results with limited resolution and frame rates. Here, lens distortion reduction has been carried out as described by Zhang (2000) while the 3D camera projection has been calibrated through manual measurement of the camera position and through the MSAC algorithm (Subbarao and Meer, 2006) within the software MATLAB. Synchronization is obtained by triggering the camera flash of a phone and setting the frame with peak lumina value as the starting point.

2.2 Development of the Inertial Measurement Unit

The pre-packaged solutions commercially available are not suited for this type of test: the large majority of IMUs are characterized by a sampling rate of up to 400 Hz and end scale of 16g. They are used for phones, console controllers, motion capture and other low velocity applications. On the other end of the spectrum there are shock sensors, typically used in the automotive industry for crash tests. While they are characterized by sufficiently high sampling rates and end scales, they are also too large to fit within an artificial boulder or to attach to a wire mesh without modifying its behaviour. The system proposed herein is constituted by three portions: (i) the sensors, (ii) the microprocessor and (iii) the power supplier. The accelerometer and gyroscopes chosen are a very affordable solution for the required metering range, following Caviezel et al. (2018b). In order to avoid soldering and low-level circuit development, pre-made evaluation boards have been used instead: STEVAL-MKI153V1 for the accelerometer and Gyro-5-click (MIKROE-3669) for the gyroscope. These breakout

boards can be connected using either Inter-Integrated Circuit (I2C) or Serial Peripheral Interface (SPI) Master-Slave serial protocols. Without going into details, the main advantage of I2C is that it only requires 2 wires: Serial Data (SDA) and Serial Clock (SCK). All the data is sent to the SCA pin on different memory addresses, meaning adding a new device only requires connecting it to the SDA and SCK pins. On the other hand, SPI requires 4 wires: Master Out Slave In (MOSI), Master In Slave Out (MISO), Chip Select (CS) and SCK. Since SPI has one input and one output wire each, MOSI and MISO, respectively, the transmission speed is significantly higher, 10 Mbps vs 5 Mbps. However, it also means adding extra slave devices, i.e. sensors, requires additional CS pins. While this is not a limitation for this specific acquisition system, I2C was chosen over SPI early in the development stage to allow for successive changes. The two sensors are connected to a RJ45 breakout board, which is the standard female connector for Ethernet cables. This type of connection has been chosen due to its extreme versatility: Ethernet cables are inexpensive, provide fast data transmission and shielding to reduce interference. The wires are doubled up to the eight internal wires of the cable to improve the signal to noise ratio. Additionally, an I2C extender (LTC4311) is placed on the main body of the acquisition system, which monitors the SCL and SDA lines. This is done to allow the acquisition system to be placed at a distance up to 30 meters from the sensors, while maintaining a good signal to noise ratio. When the signal is pulled up through the I2C resistors, the extender activates and dumps in some current to give it a boost. All the components are connected with a prototype board, which is then glued or screwed into a small container. The microcontroller is constituted by an ESP-32 devkit: (i) it has exposed pins for both I2C and SPI, digital (General-purpose input/output, GPIO) and analogical (Analog-digital converter, ADC), (ii) it integrates WiFi and Bluetooth protocols and (iii) it has the same structure of the extremely popular Arduino open-source electronic prototyping platform, meaning there are a myriad of examples and tutorials for beginners available online. Another advantage is that the GPIO pins on the ESP32 have an output of 3.3V, while other boards, such as the Arduino Uno, output to 5V. This means it interfaces directly with the sensors without needing to level shift while retaining the high number of pins and computational power. The data recorded by the instruments is stored in the microSD through ASCII files, while the Real Time Clock (RTC) module provides the timestamp to synchronize the data at a later date. Finally, the system is powered (5V) through the microUSB port of the ESP32, which means for indoor tests it can be connected to a computer, while a standard power bank for smartphones can be used on the field. A rocker switch is used to activate the instrument and three LEDs provide feedback on the system status. Table 1 lists the sensor components.

Function	Part	Details
Microcontroller	ES ESP32	5V & 3.3V DC, 320 KiB SRAM, I2C & SPI
Storage	MicroSD Module	5V DC, SPI interface
Clock	RTC1302	3.3 DC, SPI interface
I2C Extender	LTC4311	5V 7 3.3 DC, 10K pullup SCL/SDA
Accelerometer	ST H3LIS331DL	2.16V to 3.6V DC, Triax 400g 1kHz 12 bit
Gyroscope	IS ITG-3071	1.71V to 3.6V DC, Triax 4000 deg/s, 32kHz, 16 bit
Power supply	Power bank / USB port	5V DC

Table 1: Selected components for the IMU sensor.

The accelerometer is calibrated with a tumble test: assuming its response is linear, the equation $y = mx + q$ is fitted by rotating the accelerometer along its axes, so that m is the half difference between the output values obtained at $\pm 1g$, while the offset q is the average of the value obtained when the sensor is oriented on a different axis. The gyroscope is calibrated in the same way, but instead of using its orientation, it is placed on top of a stepper motor, controlled from the same ESP32.

The displacement of the IMU sensor is obtained through *deadreckoning*: double integration in the time domain after removing the gravity acceleration, low-pass filtering (Butterworth S., 1930) and linear detrending (Kok, Hol and Schön, 2017). Herein, the sensor orientation is obtained through six-axial Kalman filtering (MEMS Industry Group, 2016) within MATLAB.

3. Validation

The data acquisition system is validated by comparing (i) 3D continuous LIDAR data and discrete target displacement on the deformed cloth and (ii) 1D data from the IMU sensor and target tracking. The cloth is placed at approximately 2 meters from the LIDAR scanner (RIEGL VZ-1000) (Fig.2). A total of 6 targets, red table-tennis balls, Fig. 1, are used to track the discrete displacements of the cloth, with the IMU sensor being attached on the back of the mesh in proximity to the central target, shown in yellow in Figure 3. In the quasi-static cloth deformation test, it is possible to carry out a scan of the surface after it has been deformed, obtaining the 3D surface and the position in space of the target with high accuracy and precision. For this test, two cameras, 60 fps at 1080p, are placed at a distance of 2 meters, with an angle θ of 60 degrees between each other and the cloth. Regarding the IMU sensor, integrating the gyroscope data on the Y axis, the result is a rotation of 55 degrees, which is consistent with that obtained from the 2D section of the LIDAR data. However, computing the displacement from accelerometer data results difficult due to the small entity of the accelerations: a displacement of ≈ 22 cm over a time of 3.5 seconds means an average acceleration value of approximately 0.15 m/s^2 , on the same magnitude of noise. Further details are available in Previtali et al., (2023). The discrete displacements and errors from LIDAR and Image Analysis are reported in Table 2.

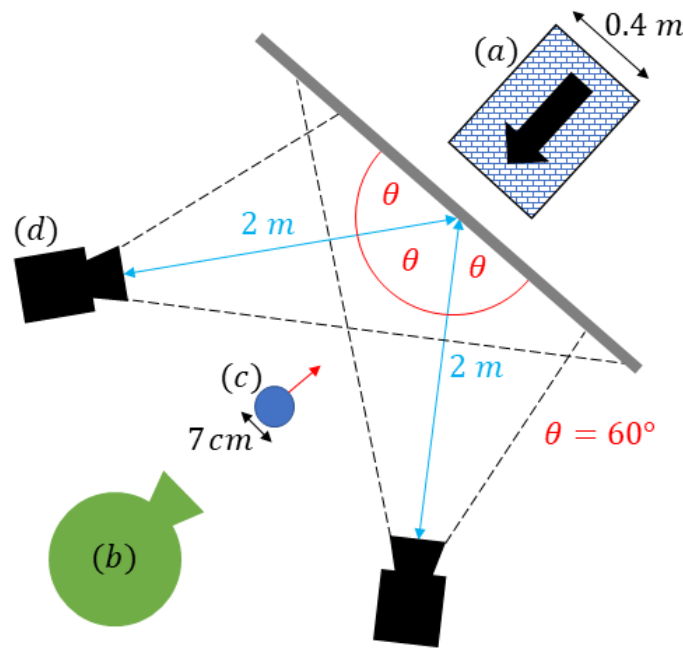


Figure 2: Scheme of the test. (a) Box used for the cloth displacement during the quasi-static test, (b) LIDAR Scanner, (c) Tennis ball used during the impact test, (d) Cameras.

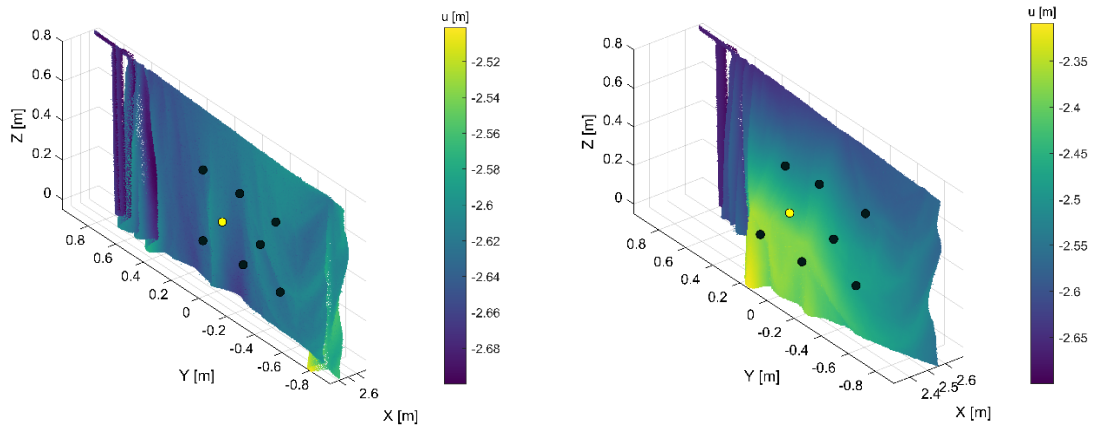


Figure 3: Point cloud data of the barrier before and during the quasi-static displacement test. The targets are shown with black dots. The IMU sensor overlaps with one of the targets and it is highlighted in yellow.

During the impact test, the ball hits the cloth roughly 15 cm to the bottom right of the target/IMU sensor, i.e. the yellow marker in Fig.3. The peak mesh acceleration being in the order of 3g, while the gyroscope data, Fig.4, shows a maximum rotation of 20 degrees on the Z axis. The LIDAR 1D time-displacement profile is obtained from the time-displacement matrix as a row corresponding to $Z = 0.5$ m, Fig.5. The different approaches are compared in Fig.6. The LIDAR data appears to be much noisier than the rest, as it corresponds to a set of laser passes between two constant angles in the Y axis, i.e. it does not follow the marker/IMU sensor, meaning slightly different portions of the cloth are captured at each pass. For this same reason, it does not follow the impact wave and the post-peak displacement bounces back in the other direction. The IMU and Image Analysis data have different peaks, possibly due to out-of-plane displacements toward the end of the braking phase. Once this phase ends, the IMU and Image analysis datasets both return to zero.

	Point 1	Point 2	Point 3	Point 4	Point 5	Point 6
X LIDAR [m]	2.6	2.59	2.6	2.61	2.6	2.62
Y LIDAR [m]	-0.45	-0.43	-0.15	0	0.13	0.12
Z LIDAR [m]	0.15	0.5	0.51	0.3	0.14	0.5
ΔX LIDAR [mm]	-135.7	-38.8	-120.5	-188.3	-257	-117.4
ΔY LIDAR [mm]	3.0	28.2	2.0	7.4	-6.0	-8.3
ΔZ LIDAR [mm]	24.3	2.4	46.7	62.9	76.5	25.2
ΔX IMG [mm]	-165.7	-69.0	-110.2	-206.7	-253.4	-108.4
ΔY IMG [mm]	3.7	12.9	3.5	7.2	-6	-9.5
ΔZ IMG [mm]	20.3	-30.0	38.0	79.4	83.5	24.1
Total error [mm]	34.7	73.1	20.5	35.1	10.6	11.3

Table 2: Discrete displacements of the targets

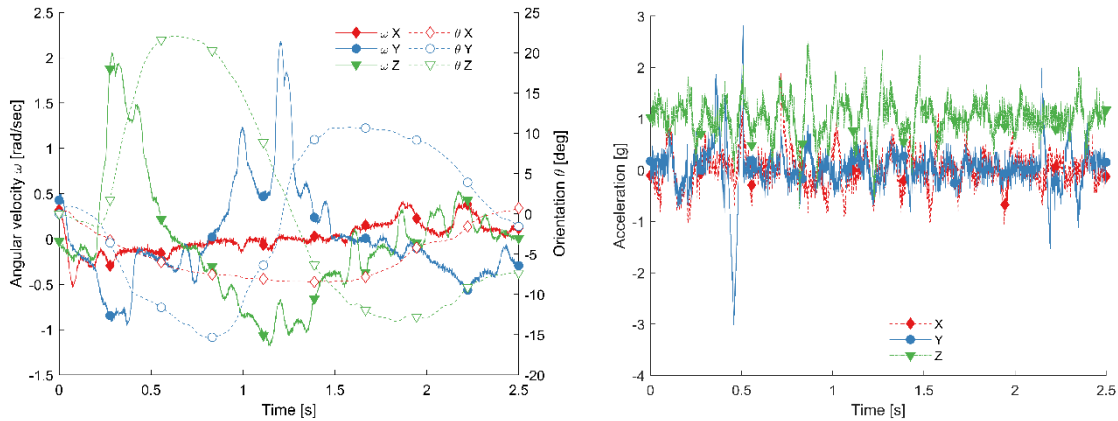


Figure 4 On the left, time-evolution of the IMU sensor spin and orientation. On the right, accelerometer data.

4. Conclusions

In this paper, a procedure to obtain the dynamic deformation of a surface is described. The simplification of the geometry into a series of targets tracked using Open-Source PTV tools instead of cross-correlation based approaches (e.g. PIV/DIC) or photogrammetry allows the usage of cheap hardware to carry out unconstrained reconstruction. For cases in which the deformation prevents continuous tracking, a list of inexpensive MEMS-based breakout boards is given, allowing end-users from different disciplines to assemble an high sampling frequency / scale IMU sensor without the requirement of soldering and knowledge of communication protocols. The use of IMU sensors is especially suited for impact experiments, as drift cumulation is insignificant throughout the test. The two examples provided have been validated against ToF LIDAR data, showing a good match for both quasi-static 3D data and 1D dynamic data.

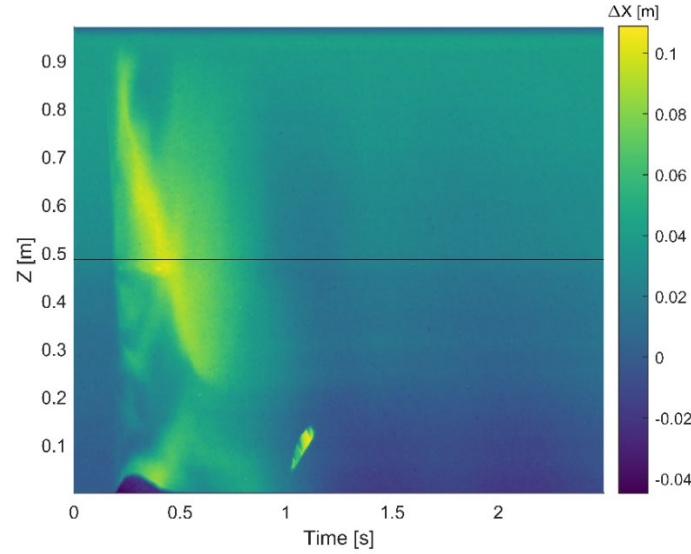


Figure 5: Time-evolution of the cloth profile in the position of the marker. Note the bottom of the cloth being lifted between $t = 0.25\text{s}$ and $t = 0.5\text{s}$ and the ball passing in front of the LIDAR beam after bouncing off at $t = 1\text{s}$. The black line represents the initial height of the target/IMU sensor.

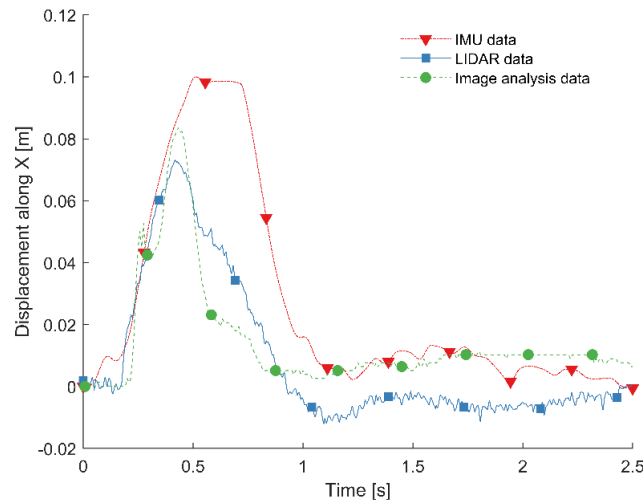


Figure 6: Displacement in the direction of the barrier normal measured with the three different approaches.

Data availability

The codes described in the paper, the connection scheme and the experimental data is available at gitlab.com/m.previtalli.

References

- Bradski, G. (2000) 'The OpenCV Library', Dr Dobb's Journal of Software Tools.
- van den Branden Lambrecht and Christian J (2001) 'Vision Models and Applications to Image and Video Processing', Vision Models and Applications to Image and Video Processing
- Bruno, N. et al. (2020) 'A comparison of low-cost cameras applied to fixed multi-image monitoring systems'. <https://doi.org/10.5194/isprs-archives-XLIII-B2-2020-1033-2020>.
- Butterworth, S. (1930). "On the Theory of Filter Amplifiers". Experimental Wireless and the Wireless Engineer. 7: 536–541.

- Buzzi, O. et al. (2013) 'Experimental testing of rockfall barriers designed for the low range of impact energy', *Rock Mechanics and Rock Engineering*, 46(4), pp. 701–712. <https://doi.org/10.1007/s00603-012-0295-1>.
- Caviezel, A. et al. (2019) 'Reconstruction of four-dimensional rockfall trajectories using remote sensing and rock-based accelerometers and gyroscopes', pp. 199–210.
- Coombs, S.P. et al. (2019) 'Mobility of dry granular flows of varying collisional activity quantified by smart rock sensors', *Canadian Geotechnical Journal*, pp. 1–13. <https://doi.org/10.1139/cgj-2018-0278>.
- EOTA (2013) 'ETAG 027:2013 Falling Rock Protection Kits', (December 1988).
- Ferrero, A.M., Segalini, A. and Umili, G. (2015) 'Experimental tests for the application of an analytical model for flexible debris flow barrier design', *Engineering Geology*. <https://doi.org/10.1016/j.enggeo.2014.12.002>.
- Gao, Z., Al-Budairi, H. and Steel, A. (2018) 'Experimental testing of low-energy rockfall catch fence meshes', *Journal of Rock Mechanics and Geotechnical Engineering*, 10(4), pp. 798–804. <https://doi.org/10.1016/j.jrmge.2018.01.004>.
- Guccione, D.E. et al. (2020) 'EFFICIENT MULTI-VIEW 3D TRACKING OF ARBITRARY ROCK FRAGMENTS UPON IMPACT'. Available at: <https://doi.org/10.5194/isprs-archives-XLIII-B2-2020-589-2020>.
- Hibert, C. et al. (no date) 'Machine learning prediction of the mass and the velocity of controlled single-block rockfalls from the seismic waves they generate'. Available at: <https://doi.org/10.5194/egusphere-2022-522>.
- Kok, M., Hol, J.D. and Schön, T.B. (2017) 'Using Inertial Sensors for Position and Orientation Estimation', *Foundations and Trends in Signal Processing*, 11(2), pp. 1–153. <https://doi.org/10.1561/20000000094>.
- MEMS Industry Group (2016) Open Source Sensor Fusion. <https://github.com/memsindustrygroup/Open-Source-Sensor-Fusion>.
- Munkres, J. (1957) 'Algorithms for the Assignment and Transportation Problems', <http://dx.doi.org/10.1137/0105003>, 5(1), pp. 32–38. <https://doi.org/10.1137/0105003>.
- Niklaus, P. et al. (2017) 'StoneNode : A Low-Power Sensor Device for Induced Rockfall Experiments', 2017 IEEE Sensors Applications Symposium (SAS), pp. 1–6. <https://doi.org/10.1109/SAS.2017.7894081>.
- Pieš, M. and Hájoský, R. (2018) 'Use of accelerometer sensors to measure the states of retaining steel networks and dynamic barriers', *Proceedings of the 2018 19th International Carpathian Control Conference, ICC 2018*, pp. 416–421. <https://doi.org/10.1109/CARPATHIANCC.2018.8399666>.
- Previtali, M., Ciantia, M. O., Spadea, S., Castellanza, R. P. & Crosta, G. B., 1 Oct 2021, 'Multiscale modelling of dynamic impact on highly deformable compound rockfall fence nets'. In: *Proceedings of the Institution of Civil Engineers: Geotechnical Engineering*. 174, 5, p. 498-511 14 p.
- Previtali, M (2023). Experimental and numerical characterization of Double-Twisted hexagonal meshes for rockfall protection. University of Dundee, Dundee, UK.
- Subbarao, R. and Meer, P. (2006) 'Beyond RANSAC: User Independent Robust Regression', in *Conference on Computer Vision and Pattern Recognition Workshop*, pp. 101–111.
- Thoeni, K. et al. (2013) 'Discrete modelling of hexagonal wire meshes with a stochastically distorted contact model', *Computers and Geotechnics*, 49, pp. 158–169. <https://doi.org/10.1016/J.COMPGE.2012.10.014>.
- Yan, Y. et al. (2019) 'Monitoring and early warning method for a rockfall along railways based on vibration signal characteristics', *Scientific Reports*, 9(1), pp. 1–10. Available at: <https://doi.org/10.1038/s41598-019-43146-1>.
- Zhang, Z. (2000) 'A flexible new technique for camera calibration', *IEEE Transactions on Pattern Analysis and Machine Intelligence*, 22(11), pp. 1330–1334. <https://doi.org/10.1109/34.888718>.